J Nanopart Res (2021) 23: 31
https://doi.org/10.1007/s11051-021-05142-3

RESEARCH PAPER

Synthesis, characterization and ab initio study of WO_3 nanocubes with peculiar electrochemical properties

A. K. H. Bashir · R. Morad · A. C. Nwanya · M. Akbari · J. Sackey · K. Kaviyarasu · I. G. Madiba · F. I. Ezema · M. Maaza

Received: 4 August 2020 / Accepted: 4 January 2021 / Published online: 29 January 2021

Abstract A non-energy intense route was used for the synthesis of highly crystalline WO_3 nanocubes. The morphological studies confirmed the cuboidal shape of the nanocrystals. Raman spectrum result for the synthesized sample revealed that the vibrational modes correspond to those ones assigned to single phase stoichiometric WO_3. The band gap Eg was derived based on UV-Vis diffuse reflectance result and found to be 2.58 eV, whereas the photoluminescence (PL) result confirmed the blue emission for the synthesized sample. The structural and electronic properties of the orthorhombic WO_3 were studied within the spin-polarized density functional theory (SDFT) using various functionals. Results indicated that the orthorhombic WO_3 is non-magnetic and has a direct band gap in the range of 2.15–3.75 eV which depends on the exchange-correlation functional used in the theory. The electrochemical studies showed that the nanocubes exhibited a peculiar electrochemical behaviour. In fact, the charge transfer resistances relatively enhanced which may results in decreasing the capacitance of the highly crystalline WO_3 nanocubes.

Keywords WO_3 · Nanocubes · Hydrothermal synthesis · Raman spectrum · Blue emission · Electrochemical properties · Density functional theory

This article is part of the topical collection: Nanotechnology Convergence in Africa

Guest Editors: Mamadou Diallo, Abdessattar Abdelkefi, and Bhekie Mamba

A. K. H. Bashir
Department of physics, Sudan University of Science and Technology, 11113 Khartoum, Sudan
e-mail: abashiruwc@gmail.com

A. K. H. Bashir · R. Morad · A. C. Nwanya · M. Akbari · J. Sackey · K. Kaviyarasu · I. G. Madiba · F. I. Ezema · M. Maaza
UNESCO-UNISA Africa Chair in Nanosciences/Nanotechnology Laboratories, College of Graduate Studies, University of South Africa (UNISA), Muckleneuk ridge, PO Box 392, Pretoria, South Africa

M. Maaza
e-mail: Maaza@tlabs.ac.za

A. K. H. Bashir · R. Morad · A. C. Nwanya · M. Akbari · J. Sackey · K. Kaviyarasu · I. G. Madiba · F. I. Ezema (✉) · M. Maaza
Nanosciences African Network (NANOAFNET), iThemba LABS-National Research Foundation, 1 Old Faure Road, PO Box 722, Somerset West, Western Cape 7129, South Africa
e-mail: fabian.ezema@unn.edu

Introduction

Tungsten trioxide (WO_3) is a multifunctional oxide which has been used in a wide range of scientific applications such as electrochromism (Bucha et al. 2016), gas sensor (Stankova et al. 2006), photo-catalysis (Li et al. 2010) and electrochemistry (Nwanya et al. 2014). Although most of the transition metal oxides are commonly used in these applications, but the importance of WO_3 arises from the fact its growth equally in all these fields in addition to chromic properties. Hence, the synthesis and analysis of WO_3 in nano-scale has become

increasingly required because it can improve the performance of this important functional metal oxide and offers remarkable properties that do not exist in its bulk form. In this nano-domain, increased surface-to-volume ratio of WO_3 particles provides more surface area for both chemical and physical interactions compared to their bulk counterpart.

WO_3 is an important n-type semiconductor with a wide band gap. The band gap of nano-scaled WO_3 is around 2.6 eV at ambient conditions (Wang et al. 2019), which is blue shifted. Such band gap facilitates the potential usage of nano-scaled WO_3 for various optical applications, especially in photocatalysis and chromism. On other hand, nano-scale can enhance the electrochemical performance of WO_3; this is due to the small distance over which the lithium ions will diffuse as well as the ion insertion and store are higher without causing degradation in the electrode (Christou et al. 2015). Nanomaterials with low dimension morphologies, i.e., 1D and/or 2D, can provide good physical and chemical properties. Since the properties of WO_3 are strongly dependent on structure, size and shape, controllable synthesis is required. Hence, several methods have been devoted for the synthesis of WO_3 nanoparticles such as template-assisted growth (Sadakane et al. 2008), anodization (Mozalev et al. 2008), thermal evaporation (Cao et al. 2009), chemical vapour deposition (Blackman and Parkin 2005), arc discharge (Ashkarran et al. 2008) and pulsed laser deposition (Lethy et al. 2008). Among these methods, hydrothermal method (Wang et al. 2019) has attracted great attention by scientists due to its advantages such as simplicity, low-cost, accuracy and low growth temperatures. However, using above methods, WO_3 with particular morphologies has been obtained including two-dimensional shapes such as nanoplates (Yang et al. 2012), nanocubes (Wang et al. 2019) and nanosheet (Azam et al. 2018).

Recently, two-dimensional nanomaterials have attracted a lot of attention due to their supreme advantages such as high surface energies and large light exposed surface area (Kumar et al. 2018). In this work, based on the advantages of two-dimensional nanomaterials, we have successfully synthesized WO_3 nanocubes using a facile hydrothermal route. The structure, morphology, optical and electrochemical properties were analysed for the highly crystalline WO_3 nanocubes. In addition, first-principle calculations based on density functional theory (DFT) (Kohn et al. 1996) was applied to study the structural and electronic properties of orthorhombic phase of WO_3. In this work, the lattice constants and the band gap were theoretically obtained through the standard DFT/GGA calculations using PBE (Perdew et al. 1996), PW91 (Perdew et al. 1992), and BLYP (Becke 1988; Lee et al. 1988) functionals as well as two hybrid functionals including B3LYP (Becke 1993; Stephens et al. 1994; Heyd et al. 2003; Giannozzi et al. 2009) and HSE (Zheng et al. 2011). Theoretical results were compared with experimental data.

Experimental details: hydrothermal synthesis of WO_3 nanocubes (NCs)

The chemical reagents used in the synthesis procedure of the WO_3 NCs were of high purity (99.99%) and used without further purification. In all the synthesis steps and washing of the synthesis product, distilled water was used. Sodium tungstate dihydrate powder ($Na_2WO_4.2H_2O$) was used as a precursor for the synthesis of WO_3 NCs. In a typical synthesis process, 1 g of ($Na_2WO4{\cdot}2H_2O$) was dissolved into 20 ml of distilled water in a glassy beaker and a HCl (8 mol/L) solution was added drop wise until the pH of the mixture was adjusted to be around 2. The mixture was kept under continuous stirring for 40 min at room temperature and ambient pressure to form a $WO_3{\cdot}H_2O$ (Wang et al. 2019). The hydrothermal synthesis was performed by transferring the mixture into a 40-mL Teflon-lined stainless steel autoclave at 200 °C for 24 h. Then, the product was let to cool down naturally at room temperature, and the precipitates were filtered and washed with distilled water and ethanol for several times before drying at 70 °C for 10 h. The hydrothermal synthesis of WO_3 could be simply described by the two following equations:

$$Na_2WO_4 + HCl + nH_2O \Rightarrow H_2WO_4 \cdot nH_2O + 2NaCl \quad (1)$$

$$H_2WO_4 \cdot nH_2O + 2NaCl \Rightarrow^{200^0C} WO_3NCs \quad (2)$$

Based on the above chemical reactions described by Eqs. (1 and 2), one can realize that this synthesis method can be considered as one-step synthesis as well as non-extensive energy method. In addition, the accuracy in the formation of highly crystalline WO_3 nanocubes in a regular or uniform manner. All these advantages make this hydrothermal method useful and effective for synthesis nanoparticles compared to some other

conventional methods which may require high growth temperature.

Characterization techniques

To identify phase and crystallography of the sample, XRD analysis was performed using a Bruker AXS D8 Advance with radiation ($\lambda_{Cuk} = 1.5406$ Å). A T64000 micro-Raman spectrometer (HORIBA Scientific, Jobin Yvon Technology) with a 532-nm laser wavelength and spectral acquisition time of 120 s was used for Raman spectrum measurement of the sample. UV-Vis reflectance spectrum was recorded for the sample using Cary 5000 UV-Vis-NIR spectrophotometer with double beam. The morphological characterization and elemental compositions of the sample were performed using Zeiss crossbeam 540 FEG SEM and high resolution transmission electron microscopy (Tecnai 720). Electrochemical studies were performed using an Autolab potentiostat equipped with NOVA 2.0 software.

Computational methods

The ab initio calculations based on the density functional theory (DFT) carried out with the Quantum Espresso (Kohn et al. 1996; Giannozzi et al. 2009) package using the plane-wave basis sets and the Norm-Conserving pseudopotentials. Different functionals including the generalized gradient approximation (GGA) PBE, PW91 and BLYP as well as two hybrid functionals including B3LYP (Becke 1993; Stephens et al. 1994) and HSE (Heyd et al. 2003) were implemented to study the structural and electronic properties of the orthorhombic WO_3. The percentage of exact Hartree-Fock (HF) exchange in B3LYP and HSE was 25%. A cut-off energy of 550 eV was used for the plane-wave basis set. The convergence threshold for the electronic structure was considered 10^{-6} Ry. A Monkhorst-Pack k-point sampling of $2 \times 2 \times 2$ with a smearing with a Gaussian broadening of 0.01 was used for the structural optimization. For the density of state calculations, a more accurate k-mesh was used.

First, we fully optimized both the lattice parameters (the volume and shape) and the atomic coordinates until all the forces on each ion were less than 0.0005 eV/Å. Then, we calculated the band gap of the fully optimized structure.

It is clear that the structure and the size of WO_3 have an important effect on its properties, including the band gap. Therefore, in order to compare with the experiment, we adapted the lattice constants from the XRD analysis and just optimized the position of atoms inside the unit-cell using DFT with the PBE and BLYP functionals. Then, the band gap was computed for the relaxed atoms.

Results and discussion

Crystal structure

As a preliminary step for characterizing our hydrothermally synthesized WO_3 NCs, we had performed the X-ray diffraction (XRD) measurement at room temperature (RT). It is evident from literature that nanostructured WO_3 has various crystal structures depending on synthesis process and/or annealing temperature. These crystal structures include monoclinic I (γ-WO_3), monoclinic II (ε-WO_3), orthorhombic (β-WO_3), tetragonal (α-WO_3) and cubic WO_3 (Zheng et al. 2011). However, it is clear from Fig. 1 that the XRD pattern of our sample indicates the presence of orthorhombic phase of WO_3, which is consistent with the (JCPDS file no. 71-2141). Accordingly, we carried out Rietveld refinement on the XRD data based on orthorhombic structure of WO_3 using *TOPAS Academy* software (Bashir et al. 2016). The space group setting used for the Rietveld refinement was *Pnma* (No.62). The solid red line in Fig. 1 represents the calculated data whereas the circular symbols with the cyan colour represent the experimental data. It can be seen from Rietveld refinement that the calculated XRD profile matches well with the experimental data

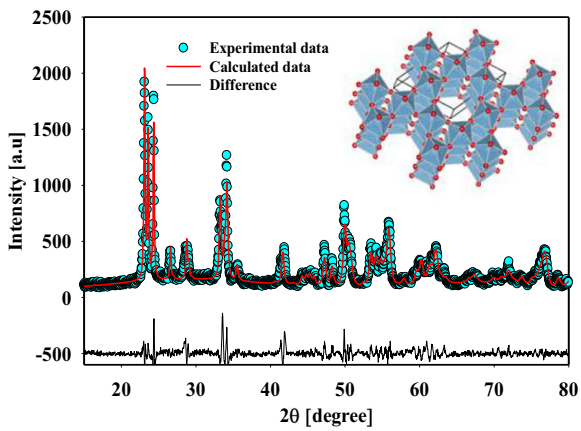

Fig. 1 XRD pattern of the synthesized WO_3 NCs

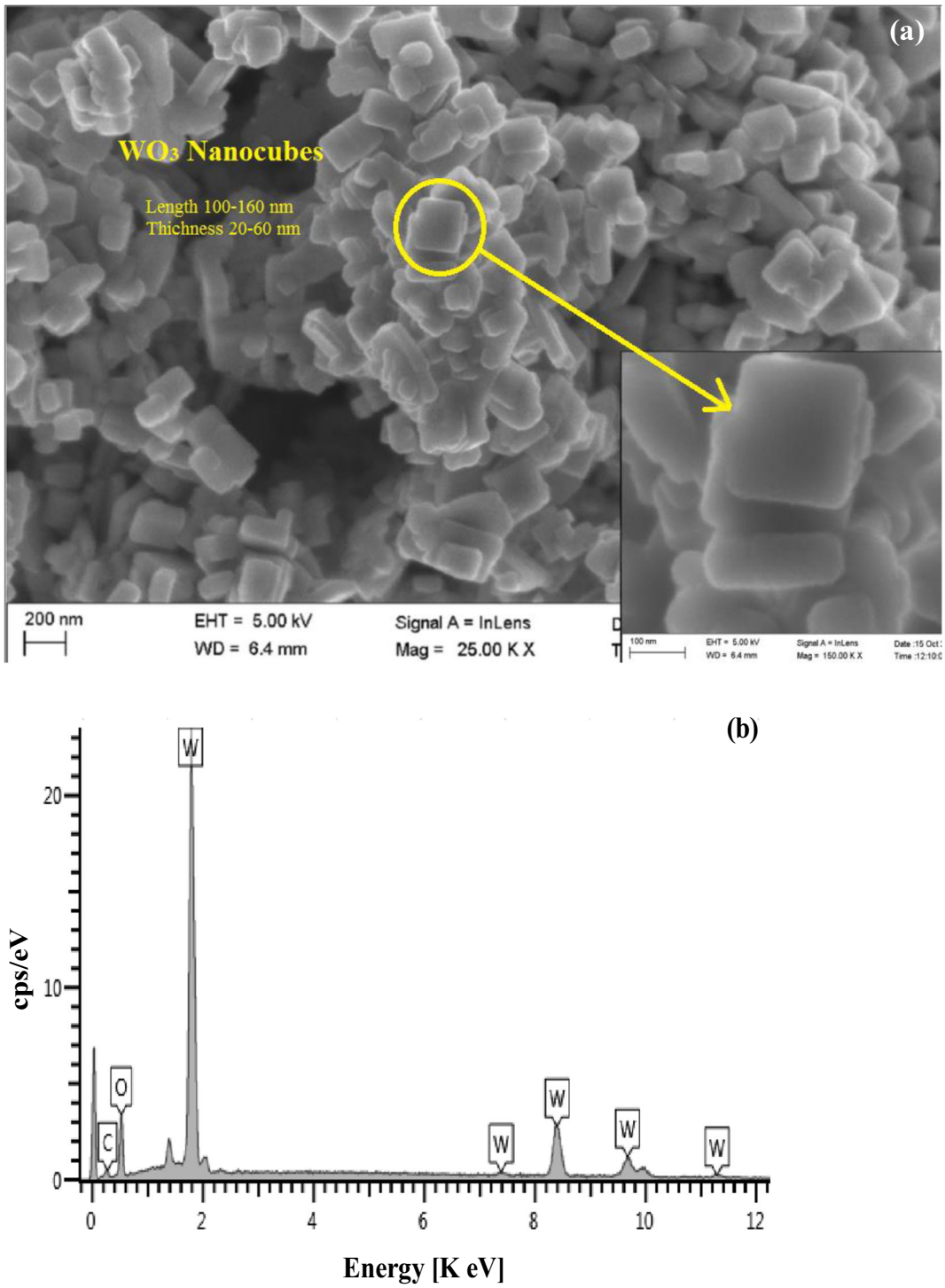

Fig. 2 **a** FESEM images of the synthesized WO_3 NCs. **b** EDS spectrum

across the entire range of measured angles which confirm the pure orthorhombic structure of WO_3 NCs. The crystal lattice constants a, b and c of the synthesized WO_3 NCs calculated from the Rietveld method were found to have the values 7.53889 Å, 7.69278 Å and 7.30659 Å, respectively. The inset of Fig. 1 displays the

crystal structure with atomic position of WO_3, showing WO_6 octahedral and vacant sites. On the other hand, the sharp diffraction peaks of the XRD pattern reflect the good crystallizing of the synthesized sample. Moreover, no impurities' peaks have been observed in the XRD pattern.

Morphological analysis

The morphology of synthesized WO_3 NCs were studied using field-emission scanning electron microscopy (FESEM). Figure 2a displays the FESEM images of the synthesized sample in low and high magnifications. Both FESEM images show the nanocube structure of our sample of large dimension. The length and thickness of the nanocube were estimated using Image-J software and were found to be 100–160 nm and 20–60 nm, respectively. Also, electron dispersive X-rays spectroscopy EDS was used in order to check the elemental compositions of the synthesized sample and to confirm the absence of contamination during the hydrothermal synthesis. Figure 2b shows the EDS spectrum which revealed that the synthesized sample is only formed by W and O elements. The appearance of C element in the spectrum is due to the carbon-coated grid used during the measurement process.

Raman spectrum analysis

To further investigate the structure and vibrational modes of the synthesized WO_3 NCs, Raman spectrum was recorded. The measurement of the spectrum was performed at ambient conditions using laser source of 532 nm for the excitation the sample. Figure 3 shows

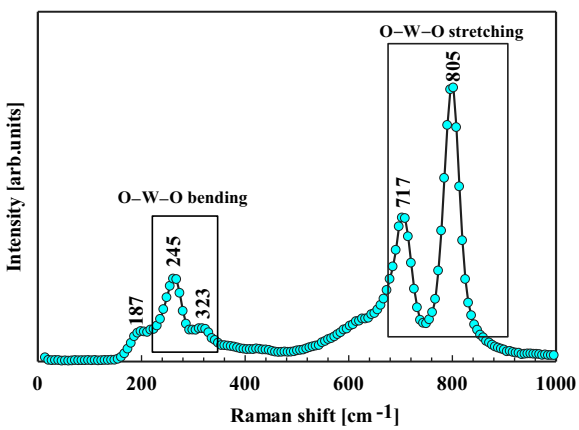

Fig. 3 Raman spectrum of the synthesized WO_3 NCs

Raman spectrum recorded for WO_3 NCs which revealed five Raman peaks. It was evident from literature that most of the vibrational modes of WO3 lattice are associated with stretching (ν), the bending (α), and the out-of-plane wagging (γ) modes (Garcia-Sanchez et al. 2013). However, the five Raman peaks of the synthesized WO_3 NCs are located at 805 cm^{-1}, 717 cm^{-1}, 323 cm^{-1}, 245 cm^{-1} and 187 cm^{-1}. The peaks located at 805 cm^{-1} and 323 cm^{-1} correspond to the stretching of O–W–O, while the peaks located at 717 cm^{-1} and 245 cm^{-1} are associated with the stretching of W–O, and the bending of O–W–O (Pecquenard et al. 1998; Habazaki et al. 2002), respectively. Finally, the peak below 200 cm^{-1} which located at 187 cm^{-1} is attributed to $(W_2O_2)_n$ chains (Pecquenard et al. 1998). It should be noted that the out-of-plane wagging (γ)(O–W–O) modes at 670 cm^{-1} is not presented in Raman spectrum of the synthesized WO_3 NCs, which can be attributed to high temperature (Garcia-Sanchez et al. 2013) that was used in hydrothermal synthesis process.

Optical properties

The optical properties such as band edge absorption, band gap and emission band peak of the synthesized WO_3 NCs were determined using UV-vis and PL techniques. Figure 4a exhibits the UV-vis diffuse reflectance spectrum of the synthesized WO_3 NCs measured at RT and in wavelengths range of 200–800 nm. It should be noted that a linear increase of the reflectance spectrum occurred in the wavelength between 450 and 500 nm before it tends to saturation. This gives strong evidence that the band edge absorption of WO_3 NCs is located around 450 nm, which is at visible light region. The band gap of the synthesized WO_3 NCs could be calculated based on UV-vis diffuse reflectance result using Tauc's equation (Ijeha et al. 2019) that given by:

$$(\alpha h\nu)^n = A\left(h\nu - E_g\right) \quad (3)$$

where hν is the photon energy, α is the optical absorption coefficient, A is a material-dependent constant and Eg is the energy band gap and n is an exponent which determines the type of the optical transition (Bashir et al. 2019), i.e. direct allowed, direct forbidden, indirect allowed and indirect forbidden transitions. The optical absorption coefficient of the materials is exponentially dependent on the photon energy. This is basically due to the electronic transitions occurring between localized

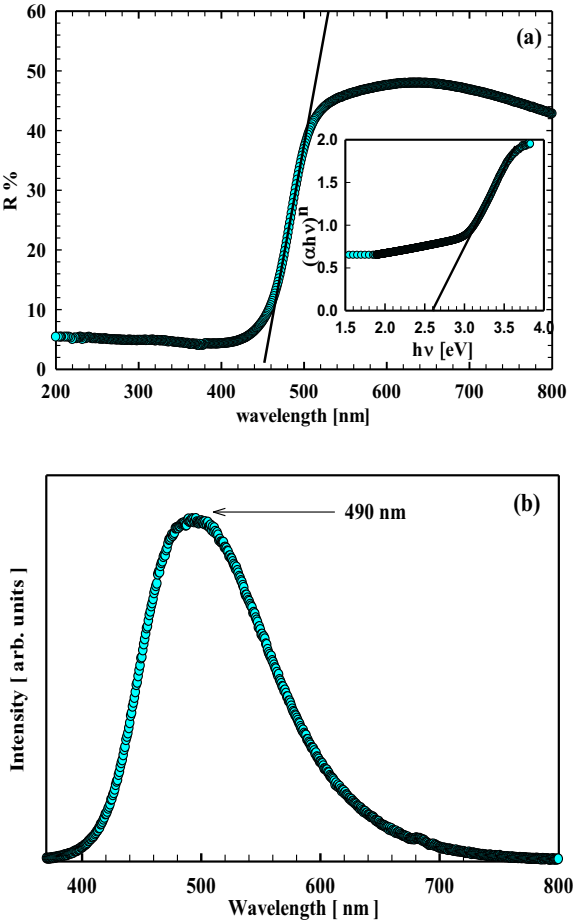

Fig. 4 **a** UV-vis diffuse reflectance spectrum of WO_3NCs. **b** PL spectrum

states which play an important role in determining the value of the energy band gap (Babu and Madhuri 2017). However, the exponent *n* takes the value of 1/2 of the indirect optical transition for WO_3 (Miyauchi 2008). Inset of Fig. 4a shows the plot of $(\alpha h\nu)^n$ against $(h\nu)$, which allows to calculate the energy gap by extrapolation of the straight-line graph at $(\alpha h\nu)^n = 0$. The band gap of the synthesized WO_3 NCs was found to be 2.57 eV which is plausible and in a good agreement with the reported previous studies (Wang et al. 2019; Miyauchi 2008).

PL spectrum exhibits only one peak centred at 490 nm which located at visible region and related to the Blue emission. The Blue emission in such materials often arises from the transitions between deep donor levels and the valence band (Bashir et al. 2020).

Table 2 The experimental data vs the calculated DFT results at the level of GGA/PBE/plane wave of the theory

Functional	a (Å)	b (Å)	c (Å)	Band gap (eV)
Exp [this work]	7.53889	7.69278	7.30659	2.58
GGA/PBE	7.53889	7.69278	7.30659	2.52
GGA/BLYP	7.53889	7.69278	7.30659	2.77

Structural and electronic properties from DFT

We studied orthorhombic WO_3 crystal structures with *Pnma* space group. The considered cell consists of 24 O and 8 W atoms. First, we fully optimized the cell with different functionals and the same norm-conserving pseudopotential from the Quantum Espresso pseudopotential library. The results of optimized lattice parameters, equilibrium volume and the band gap are listed in Table 1. Our results indicated that PW91 and HSE overestimate the equilibrium volume by 0.34% and 1.74%, respectively. While the PBE, BLYP, and B3LYP underestimate the equilibrium volume by 2.7%, 0.468 and 7.311%, respectively. Therefore, PW91 and BLYP predict the structural properties better.

The experimental band gap of WO_3 was reported in literature in the range of 2.5 to 3.2 eV (Granqvist 2000; Kharade et al. 2010; Gesheva et al. 2003; Gonzalez-Borrero et al. 2010). In our study, the hybrid functionals

Table 1 Calculated lattice parameters, equilibrium volume and band gap of the bulk orthorhombic WO3 by various DFT methods

Functional	a (Å)	b (Å)	c (Å)	Volume ($Å^3$/cell)	Band gap (eV)
Exp(Salje 1977)	7.24	7.57	7.75	53.9	
GGA/PW91	7.303	7.625	7.768	54.083	2.1547
GGA/PBE	7.142	7.602	7.719	52.393	2.6305
GGA/BLYP	7.162	7.681	7.800	53.647	2.8681
Hybrid/HSE	7.294	7.692	7.818	54.842	3.7591
Hybrid/B3LYP	7.025	7.470	7.615	49.958	5.2254

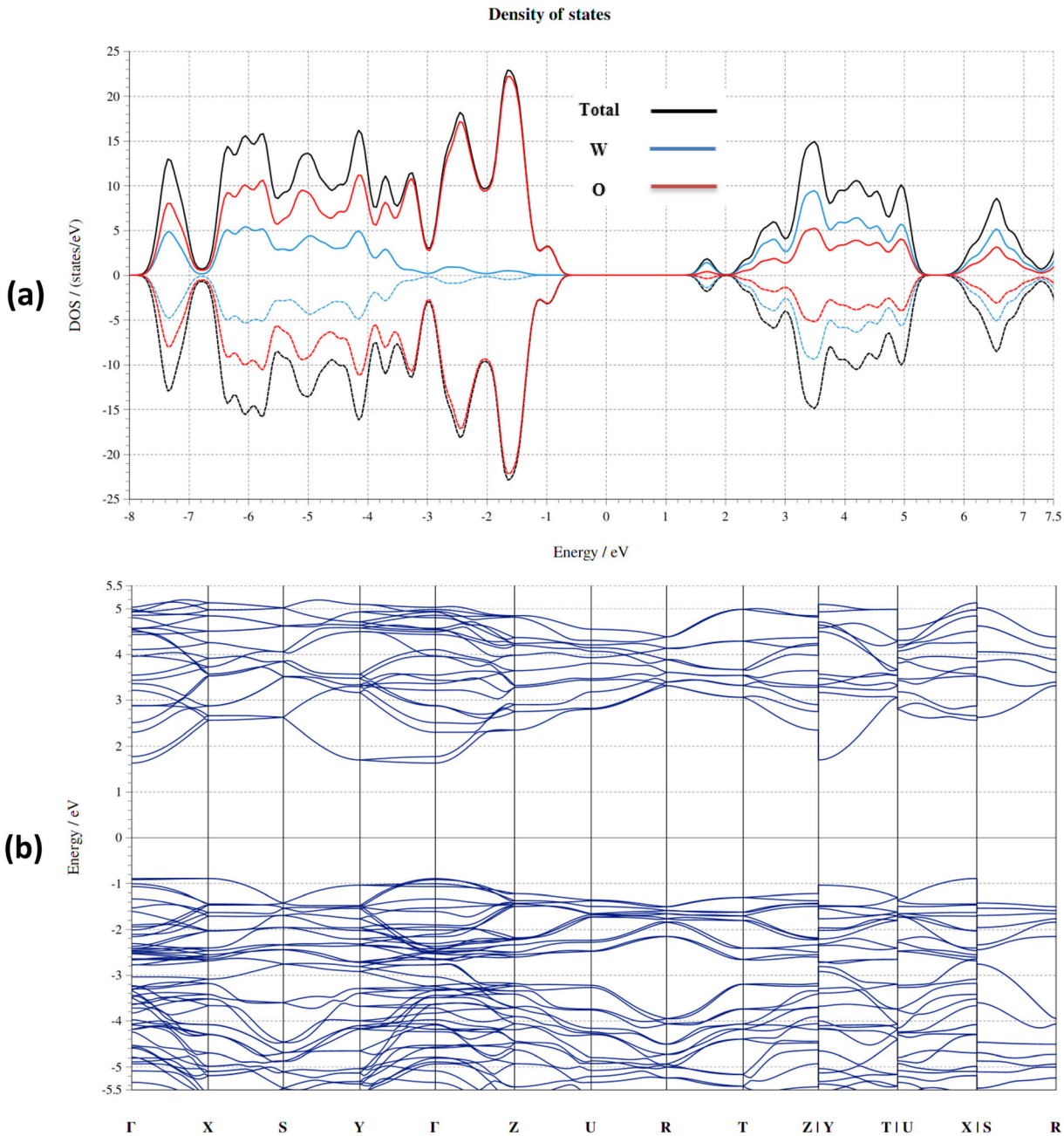

Fig. 5 **a** The electronic density of states (DOS) of the relaxed structure using SDFT with PBE functional. The black, red and blue curve shows the total, O, and W DOS. The upper and lower panels indicate the spin up and the spin down DOS, respectively. **b** The corresponding band structure

with 25% of exact HF exchange overestimate the band gap, while the GGA/PW91 underestimates the band gap. The GGA/PBE and GGA/BLYP band gap is 2.63 and 2.86 eV, respectively which is in the range of reported experiments.

This work reported the synthesis of nano-scaled WO_3 NCs with the lattice parameters reported in Table 2. In order to compare the DFT calculations with the experiment, we adapted the lattice constants from the XRD analysis and just optimized the position of atoms inside

the cell with the PBE and BLYP functionals which worked best in predicting both the structure and the band gap of bulk WO_3. The results are listed in Table 2. The band gap of PBE is 2.52 eV which is very close to our experimental value.

Figure 5 a and b show the PBE density of states (DOS) and the band structure, respectively. In this figure the Fermi energy sets to zero. The total magnetization of our spin polarized calculations of the WO_3 is zero; therefore, the density of states for spin up and down is exactly the same which indicates that the WO_3 has no magnetic moment. Also, one can see that the valence band mainly consists of the O electrons, while the valence electrons of W predominantly play a main role for the conduction band. The corresponding band structure shows that the band gap is direct at gamma point.

Electrochemical study

The cyclic voltammograms (CV) of the hydrothermally obtained WO_3 nanoparticles on glassy carbon electrode and the bare glassy carbon is as shown in Fig. 6a. The CV were obtained at 50 mV s^{-1} in 3 M KOH in the potential range of − 0.6 to 0.6 V/Ag/AgCl. It is obvious that the glassy carbon electrode contributed little or nothing to the redox process. Figure 6b shows the cyclic voltammogram at various scan rate (20–100 mV s^{-1}) indicating an enhancement in the peak current as the scan rate increases. The CV at the scan rate scan rate of 20 mV s^{-1} showed a boarder anodic peak centred at 0.24 V and a reverse narrower cathodic peak at 0.07 V. The anodic peak shifted a little bit to the positive potential at higher scan rate while the cathodic peak remained almost at the same position. This shift in the peak positions shows that the redox processes is quasi-reversible (Nwanya et al. 2020). The anodic scan leads to the de-insertion of the K^+ and the oxidation of W^{5+} to W^{6+} while the reverse cathodic scan causes the reduction of W^{6+} back to W^{5+}. The kinetics of the redox reactions were further studied using Eq. 4 (Chen et al. 2018):

$$I_{pa} = k_1\nu + k_2\nu^{1/2} \tag{4}$$

where I_{pa} is the anodic peak current, while k_1 and k_2 are respectively the capacitive and diffusion controlled contribution to the capacity. Our analysis shows the charge storage mechanism is dominated by diffusion-controlled reactions and a ratio of capacitive to diffusion-controlled capacity of 1:2 is obtained. The areal capacity was obtained from the cyclic voltammogram by integrating the absolute area under the curve using Eq. 5 (Nwanya et al. 2017):

$$Q_a = \frac{\int IdV}{A\nu} \tag{5}$$

where I, V, ν and A are respectively the current, potential window, scan rate and the area of the WO_3 on the GCE. Capacity value of 18.9 mC cm^{-2} (18.9 mF cm^{-2}; the potential window is 1 V) was obtained at a scan rate of 100 mV s^{-1}. Studies have shown that high crystalline WO_3 gives low capacities (Chen et al. 2018). Hence, the seemingly low capacity we obtained is most likely due to the high crystalline nature of the WO_3 NCs. However, the value of the areal capacitance obtained is a lot of improvement from 4 mF cm^{-2} obtained by Nwanya et al. at a scan rate of 50 mV s^{-1} (Nwanya et al. 2014). It is also comparable to 25 mF cm^{-2} obtained by Zou et al. (Zou et al. 2014) for a composite of WO_3 and polyaniline at a scan rate of 5 mV s^{-1}.

The frequency response to the mechanism of the charge storage were further studied using electrochemical impedance spectroscopy (EIS) within the frequency

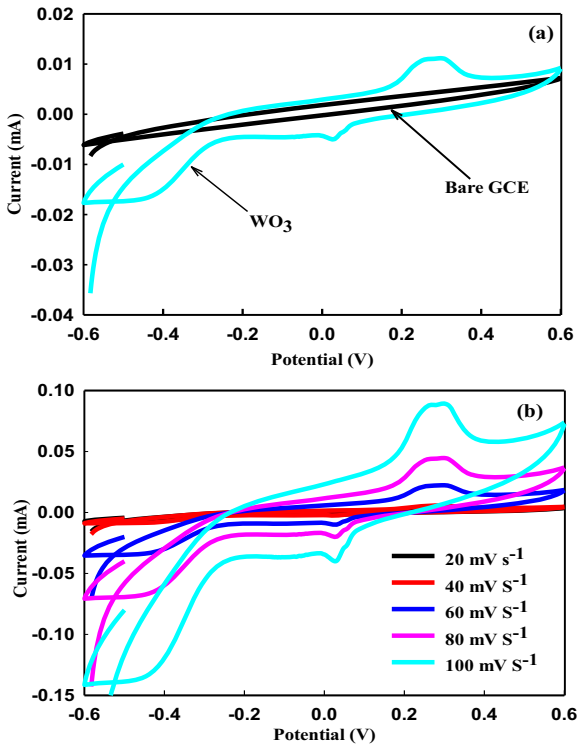

Fig. 6 Cyclic voltammetry in 3 M KOH of **a** bare GCE and GCE/WO_3 nanocomposites at 50 mV s^{-1} and **b** GCE/WO_3 nanocomposites at different scans rates (20–100 mV s^{-1})

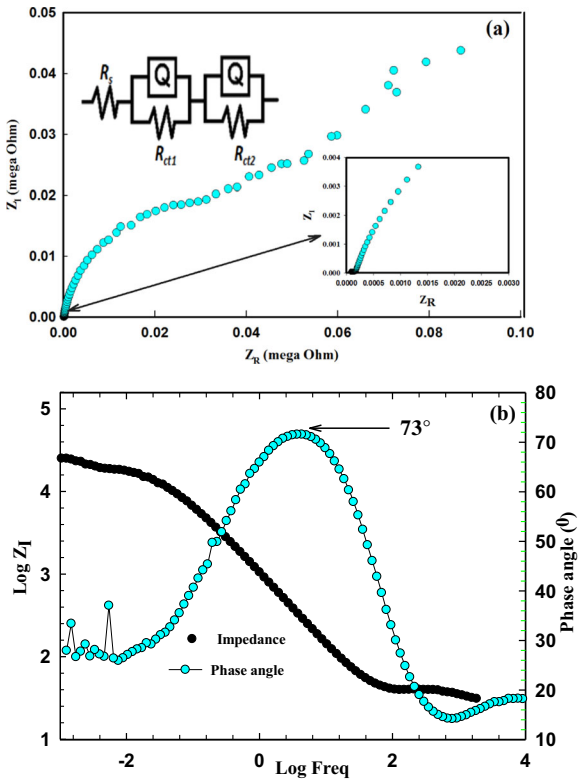

Fig. 7 **a** Nyquist plot. **b** Bode plot

range of 0.01 Hz to100 kHz at a voltage amplitude of 10 mV. The Nyquist plot (Fig. 7a) shows a distorted small semicircle (lower inset of Fig. 7a) at high frequency and terminates in a vertical line in the medium to low frequency region. The high frequency region is kinetics controlled and the distorted semicircle in this region gives the charge transfer resistances (Rct_1 and Rct_2) due to the migration of ions and electrons at the GCE/WO_3/electrolyte interfaces. The vertical line in the low frequency region is associated with the diffusion of ions to the electrode. The equivalent circuit (upper inset of Fig. 7a) and the values of the circuit elements (Table 3) were fitted using the *ZsimW in* software. The resistance to the movement of ions in the electrolyte solution is depicted as the electrolyte resistance (R_s) while the inhomogeneity which occurs at GCE/WO_3/electrolyte interfaces is represented by the constant phase element (CPE or Q). The very large values of the charge transfer resistances may indicate low value of the capacitance of the high crystalline WO_3 NCs. The bode plot (Fig. 7b) showed a phase angle of 75°, which gives an indication that the charge storage mechanism is not governed by electric double layer capacitance.

Table 3 Fitted values of circuit elements

Circuit element	Values
Rs (Ω)	131.20±4.15
Q1 (S-s)	$3.54\times10^{-5}\pm0.47\times10^{-5}$
Rct1 (MΩ)	0.14±0.02
Q2 (S-s)	$5.40\times10^{-6}\pm0.56\times10^{-6}$
Rct2 (kΩ)	223.70±2.68

Conclusion

In summary, the highly crystalline WO_3 nanocubes were synthesized via hydrothermal route at 200 °C. All characterization techniques used have confirmed the formation of WO_3 nanocubes. The analysis of the optical properties revealed that the band gap is blue shifted. The ab initio calculation in the spin-polarized DFT framework was performed to study the structural and electronic properties of bulk orthorhombic WO_3 using the plane wave QUANRUM-ESPRESSO package. Both standard DFT/GGA functionals and the hybrid functional were used in order to examine the best method to describe the bulk properties. It was found that the band gap of orthorhombic WO_3 in the GGA/PBE level of theory is 2.52 eV which is very close to the experimental value. In addition, all spin-polarized DFT calculations indicated that the orthorhombic WO_3 is non-magnetic with direct band gap. Electrochemical result showed that the charge storage mechanism is not governed by electric double layer capacitance.

Acknowledgements Authors are grateful to the UNESCO-UNISA Africa Chair in Nanosciences and Nanotechnology(U2ACN2), The High Performance Computing (HPC), College of Graduate Studies, University of South Africa, the National Research Foundation of South Africa (NRF), iThemba LABS for the financial support and facilities. A.K.H Bashir thanks UNESCO-UNISA Africa Chair in Nanosciences and Nanotechnology (U2ACN2) for the (Post-Doctoral Fellowship programme under contract number: 90396898).

Compliance with ethical standards

Conflict of interest The authors declare that they have no conflict of interest.

References

Ashkarran AA, Irajizad A, Ahadian MM, Ardakani SAM (2008) Synthesis and photocatalytic activity of W_3 nanoparticles prepared by the arc discharge method in deionized water. Nanotechnology 19:195709–195716

Azam A, Kim J, Park J, Novak TG, Tiwari AP, Song SH, Kim B, Jeon S (2018) Two dimensional WO_3 nanosheets chemically converted from layered WS2 for high performance electrochromic devices. Nano Lett 18:5646–5651

Babu MB, Madhuri KV (2017) Structural, morphological and optical properties of electron beam evaporated WO_3 thin films. J Taibah Univ Sci 11:1232–1237

Bashir AK, Tchokonte MBT, Strydom AM (2016) Electrical and thermal transport properties of $RECu_4Au$ compounds, RE=Nd, Gd. J Magn Magn Mat 414:69–73

Bashir AKH, Furqan CM, Bharuth-Ram K, Kaviyarasu K, Tchokonte MBT, Maaza M (2019) Structural, optical and Mössbauer investigation on the biosynthesized α-Fe_2O_3: study on different precursors. Phys E Low Dimens Syst Nanostruct 111:152–157

Bashir AKH, Matinise N, Sackey J, Kaviyarasu K, Madiba IG, Kodseti L, Maaza M (2020) Investigation of electrochemical performance, optical and magnetic properties of $NiFe_2O_4$ nanoparticles prepared by a green chemistry method. Phys E Low Dimens Syst Nanostruct 119:114002

Becke AD (1988) Exchange: density-functional exchange-energy approximation with correct asymptotic behavior. Phys Rev A 38(1988):3098 (subscription needed)

Becke AD (1993) B3LYP: density-functional thermochemistry. III. The role of exact exchange. J Chem Phys 98:5648 (subscription needed)

Blackman CS, Parkin IP (2005) Atmospheric pressure chemical vapor deposition of crystalline monoclinic WO_3 and WO_{3-x} thin films from reaction of WCl6 with O-containing solvents and their photochromic and electrochromic properties. Chem Mater 17:1583–1590

Bucha VR, Chawlab AK, Rawalc SK (2016) Review on electrochromic property for WO_3 thin films using different deposition techniques Mater. Today Proceed 3:1429

Cao B, Chen J, Tang X, Zhou W (2009) Growth of monoclinic WO_3 nanowire array for highly sensitive NO_2 detection. J Mater Chem 19:2323–2327

Chen J, Wang H, Deng J, Xu C, Wang Y (2018) Low-crystalline tungsten trioxide anode with superior electrochemical performance for flexible solid-state asymmetry supercapacitor. J Mater Chem. A 6:8986–8991

Christou K, Louloudakis D, Vernardou D, Katsarakis N, Koudoumas E (2015) Onepot syn thesis of WO_3 structures at 95°C using HCl. J Sol Gel Sci Technol 73:520–526

Garcia-Sanchez RF, Ahmido T, Casimir D, Baliga S, Misra P (2013) Thermal effects associated with the Raman spectroscopy of WO_3 gas-sensor materials. J Phys Chem A 117: 13825–13831

Gesheva K, Szekeres A, Ivanova T (2003) Photovoltaics and photoactive materials - properties, technology and applications. Sol Energy Mater Sol Cells 76:563–576

Giannozzi P, Baroni S, Bonini N, Calandra M, Car R, Cavazzoni C, Corso AD (2009) Quantum espresso: a modular and open-source software project for quantum simulations of materials. J Phys Condens Matter 21(39):39550

Gonzalez-Borrero PP, Sato F, Medina AN, Baesso ML, Bento AC, Baldissera G, Persson C, Niklasson GA, Granqvist CG, Ferreira da Silva A (2010) Optical band-gap determination of nanostructured WO_3 film. Appl Phys Lett 96:061909

Granqvist CG (2000) Electrochromic tungsten oxide films: review of progress 1993-1998. Sol Energy Mater Sol Cells 60:201–262

Habazaki H, Hayashi Y, Konno H (2002) Characterization of electrodeposited WO3 films and its application to electrochemical wastewater treatment. Electrochim Acta 47:4181–4188

Heyd J, Scuseria GE, Ernzerhof M (2003) Hybrid functionals based on a screened Coulomb potential. J Chem Phys 118(18):8207–8215

Ijeha RO, Nwany AC, Nkeleb AC, Khumalo Z, Madiba IG, Bashir AK, Osujib RU, Maaza M, Ezema F (2019) Magnetic and optical properties of electrodeposited nanospherical copper doped nickel oxide thin films. Phys E Low Dimens Syst Nanostruct 113:233–239

Kharade RR, Mane SR, Mane RM, Patil PS, Bhosale PN (2010) Synthesis and characterization of chemically grown electrochromic tungsten oxide. J Sol-Gel Sci Technol 56:177

Kohn W, Becke AD, Parr RG (1996) Density functional theory of electronic structure. J Phys Chem 100:12974–12980

Kumar SK, Choudhary N, Jung Y, Thomas J (2018) Recent advances in two-. dimensional nanomaterials for supercapacitor electrode applications. ACS Energy Lett 3(2):482–495

Lee C, Yang W, Parr RG (1988) Correlation: development of the Colle-Salvetti correlation-energy formula into a functional of the electron density. Phys Rev B 37:785 (subscription needed)

Lethy KJ, Beena D, Mahadevan Pillai VP, Ganesan V (2008) Bandgap renormalization in titania modified nanostructured tungsten oxide thin films prepared by pulsed laser deposition technique for solar cell applications. J Appl Phys 104: 033515–033512

Li L, Krissanasaeranee M, Pattinson SW, Stefik M, Wiesner U, Steiner U, Eder D (2010) Enhanced photocatalytic properties in well-ordered mesoporous WO_3. Chem Commun 46:7620–7762

Miyauchi M (2008) Photocatalysis and photoinduced hydrophilicity of WO_3 thin films with underlying Pt nanoparticles. Phys Chem Chem Phys 10:6258–6265

Mozalev A, Khatko V, Bittencourt C, Hassel AW, Gorokh G, Llobet E, Correig X (2008) Nanostructured column like tungsten oxide film by anodizing Al/W/Ti layers on Si. Chem Mater 20:6482

Nwanya AC, Jafta CJ, Ejikeme PM, Ugwuoke PE, Reddy MV, Osuji RU, Ozoemena KI, Ezema FI (2014) Electrochromic and electrochemical capacitive properties of tungsten oxide and its polyaniline nanocomposite films obtained by chemical bath deposition method. Electrochim Acta 128:21

Nwanya AC, Obi D, Osuji RU, Bucher R, Maaza M, Ezema FI (2017) Simple chemical route for nanorod-like cobalt oxide films for electrochemical energy storage applications. J Solid State Electrochem 21:2567–2576

Nwanya AC, Ndipingwi MM, Ikpo CO, Obodo RM, Nwanya SC, Botha S, Ezema FI, Iwuoha EI, Maaza M (2020) Zea mays

lea silk extract mediated synthesis of nickel oxide nanoparticles as positive electrode material for asymmetric supercar battery. J Alloys Compd 822:153581.8–153581.15358225

Pecquenard B, Lecacheaux H, Livage L, Julien C (1998) J Solid State Chem : 135, 159-168. Habazaki H, Hayashi Y, Konno H (2002). Electrochim Acta 47:4181–4188

Perdew JP, Chevary JA, Vosko SH, Jackson KA, Pederson MR, Singh DJ, Fiolhais C (1992) Atoms, molecules, solids, and surfaces: applications of the generalized gradient approximation for exchange and correlation. Phys Rev B 46(11):6671

Perdew JP, Burke K, Ernzerhof M (1996) Generalized gradient approximation made simple. Phys Rev Lett. 77(18):3865

Sadakane M, Sasaki K, Kunioku H, Ohtani B, Ueda W, Abe R (2008) Preparation of nanostructured crystalline tungsten(VI) oxide and enhanced photocatalytic activity for decomposition of organic compounds under visible light irradiation. Chem Commun (48):6552–6556

Salje E (1977) The orthorhombic phase of WO3. Acta Crystallogr B 33:574–577

Stankova M, Vilanova X, Llobet E, Calderer J, Vinaixa M, Gracia I, Cane C, Correig X (2006) On-line monitoring of CO_2 quality using doped WO_3 thin film sensors. Thin Solid Films 500:302–308.554

Stephens PJ, Devlin FJ, Chabalowski CF, Frisch MJ (1994) Ab initio calculation of vibrational absorption and circular dichroism spectra using density functional force fields. J Phys Chem 98:11623–11627

Wang L, Hu H, Xu J, Zhu S, Ding A, Deng C (2019) WO3 nanocubes: hydrothermal synthesis, growth mechanism, and photocatalytic performance. J Mater Res 34(17):2955–2963

Yang J, Li W, Li J, Sun D, Chen Q (2012) Hydrothermal synthesis and photoelectrochemical properties of vertically aligned tungsten trioxide(hydrate) plate-like arrays fabricated directly on FTO substrates. J MaterChem 22:17744–17752

Zheng H, Ou JZ, Strano MS, Kaner RB, Mitchell A, Kalantarzadeh K (2011) Nanostructured tungsten oxide properties, synthesis, and applications. Adv Funct Mater 21: 2175–2196

Zou B, Gong S, Wang Y, Liu X (2014) Tungsten oxide and polyaniline composite fabricated by surfactant-templated electrodeposition and its use in supercapacitors. Journal of nanomaterials 2014:Article ID 813120

Terms and Conditions

Springer Nature journal content, brought to you courtesy of Springer Nature Customer Service Center GmbH (“Springer Nature”).
Springer Nature supports a reasonable amount of sharing of research papers by authors, subscribers and authorised users (“Users”), for small-scale personal, non-commercial use provided that all copyright, trade and service marks and other proprietary notices are maintained. By accessing, sharing, receiving or otherwise using the Springer Nature journal content you agree to these terms of use (“Terms”). For these purposes, Springer Nature considers academic use (by researchers and students) to be non-commercial.
These Terms are supplementary and will apply in addition to any applicable website terms and conditions, a relevant site licence or a personal subscription. These Terms will prevail over any conflict or ambiguity with regards to the relevant terms, a site licence or a personal subscription (to the extent of the conflict or ambiguity only). For Creative Commons-licensed articles, the terms of the Creative Commons license used will apply.
We collect and use personal data to provide access to the Springer Nature journal content. We may also use these personal data internally within ResearchGate and Springer Nature and as agreed share it, in an anonymised way, for purposes of tracking, analysis and reporting. We will not otherwise disclose your personal data outside the ResearchGate or the Springer Nature group of companies unless we have your permission as detailed in the Privacy Policy.
While Users may use the Springer Nature journal content for small scale, personal non-commercial use, it is important to note that Users may not:

1. use such content for the purpose of providing other users with access on a regular or large scale basis or as a means to circumvent access control;
2. use such content where to do so would be considered a criminal or statutory offence in any jurisdiction, or gives rise to civil liability, or is otherwise unlawful;
3. falsely or misleadingly imply or suggest endorsement, approval , sponsorship, or association unless explicitly agreed to by Springer Nature in writing;
4. use bots or other automated methods to access the content or redirect messages
5. override any security feature or exclusionary protocol; or
6. share the content in order to create substitute for Springer Nature products or services or a systematic database of Springer Nature journal content.

In line with the restriction against commercial use, Springer Nature does not permit the creation of a product or service that creates revenue, royalties, rent or income from our content or its inclusion as part of a paid for service or for other commercial gain. Springer Nature journal content cannot be used for inter-library loans and librarians may not upload Springer Nature journal content on a large scale into their, or any other, institutional repository.
These terms of use are reviewed regularly and may be amended at any time. Springer Nature is not obligated to publish any information or content on this website and may remove it or features or functionality at our sole discretion, at any time with or without notice. Springer Nature may revoke this licence to you at any time and remove access to any copies of the Springer Nature journal content which have been saved.
To the fullest extent permitted by law, Springer Nature makes no warranties, representations or guarantees to Users, either express or implied with respect to the Springer nature journal content and all parties disclaim and waive any implied warranties or warranties imposed by law, including merchantability or fitness for any particular purpose.
Please note that these rights do not automatically extend to content, data or other material published by Springer Nature that may be licensed from third parties.
If you would like to use or distribute our Springer Nature journal content to a wider audience or on a regular basis or in any other manner not expressly permitted by these Terms, please contact Springer Nature at

onlineservice@springernature.com